Denoising and Artefact Reduction in Dynamic Flat Detector CT Perfusion Imaging using High Speed Acquisition: First Experimental and Clinical Results

Michael T. Manhart[1,2], André Aichert[1,2], Tobias Struffert[2], Yu Deuerling-Zheng[3], Markus Kowarschik[3], Andreas K. Maier[1], Joachim Hornegger[1,4], and Arnd Doerfler[2]

[1]Pattern Recognition Lab, Department of Computer Science,
Friedrich-Alexander-Universität Erlangen-Nürnberg, Martensstr. 3, 91058 Erlangen, Germany
[2]Department of Neuroradiology, Universitätsklinikum Erlangen, Schwabachanlage 6, 91054 Erlangen, Germany
[3]Siemens AG, Angiography & Interventional X-Ray Systems, Siemensstraße 1, 91301 Forchheim, Germany
[4]Erlangen Graduate School in Advanced Optical Technologies (SAOT),
Paul-Gordan-Str. 6, 91052 Erlangen, Germany

E-mail: michael.manhart@cs.fau.de

Abstract. Flat detector CT perfusion (FD-CTP) is a novel technique using C-arm angiography systems for interventional dynamic tissue perfusion measurement with high potential benefits for catheter-guided treatment of stroke. However, FD-CTP is challenging since C-arms rotate slower than conventional CT systems. Furthermore, noise and artefacts affect the measurement of contrast agent flow in tissue. Recent robotic C-arms are able to use high speed protocols (HSP), which allow sampling of the contrast agent flow with improved temporal resolution. However, low angular sampling of projection images leads to streak artefacts, which are translated to the perfusion maps. We recently introduced the FDK-JBF denoising technique based on Feldkamp (FDK) reconstruction followed by joint bilateral filtering (JBF). As this edge-preserving noise reduction preserves streak artefacts, an empirical streak reduction (SR) technique is presented in this work. The SR method exploits spatial and temporal information in the form of total variation and time-curve analysis to detect and remove streaks. The novel approach is evaluated in a numerical brain phantom and a patient study. An improved noise and artefact reduction compared to existing post-processing methods and faster computation speed compared an algebraic reconstruction method are achieved.

Keywords: Flat Detector CT, 3D Reconstruction, Perfusion Imaging, Stroke Treatment, Noise Reduction

1. Introduction

Imaging of brain perfusion is a routine method in the emergency work-up of patients suspected to suffer from acute ischemic stroke (AIS). Commonly, CT perfusion (CTP) is used to identify stroke-affected tissue by acquiring hemodynamic information on the capillary level of the brain (Miles & Griffiths 2003). Time-concentration curves (TCCs) in tissue and vessels are extracted from a time series of CT brain volumes acquired after a contrast bolus injection. The hemodynamics are visualized by perfusion parameter maps, representing quantities such as cerebral blood flow (CBF), cerebral blood volume (CBV), mean transit time (MTT), and time-to-peak (TTP). The parameter maps provide important information about the extent of the stroke and allow for the identification of potentially salvageable ischemic tissue (penumbra). If the stroke is diagnosed in a time window of up to 4.5 hours after onset, a common treatment is intravenous (IV) thrombolytic therapy (Hacke et al. 2008). A meta analysis of stroke therapy articles (Rha & Saver 2007) showed a strong relation of successful vessel recanalization to the final clinical outcome in AIS. The meta analysis reported that the recanalization rate with IV thrombolytic therapy was approximately twice the spontaneous rate, but still less than half of all cases. Techniques to improve this modest recanalization rate are desirable.

In recent years, interventional intra-arterial (IA) stroke therapy procedures were introduced to improve the recanalization rate and the treatment outcome. Interventional treatment procedures of AIS are IA thrombolytic therapy (Furlan et al. 1999) and recanalization of occluded arteries using mechanical endovascular retrieval devices (Zaidat et al. 2008). For interventional stroke management, the patient needs to be transported to an interventional suite equipped with a C-arm angiography system. Recent generations of C-arm systems provide an option to reconstruct CT like volumes, e.g., to detect haemorrhages (Struffert et al. 2009). However, due to hardware limitations, dynamic interventional perfusion imaging is challenging and not yet clinically available. If flat detector CT could provide equal information as conventional CT regarding the brain parenchyma, the vessel status, and perfusion, then patients could be directly referred to the interventional suite, saving the time of moving the patient from a CT scanner room. Furthermore, dynamic perfusion imaging with flat detector CT (FD-CTP) would allow intraoperative monitoring of the brain perfusion. Ahmed et al. (Ahmed et al. 2009) proposed a method using a steady state contrast injection protocol to acquire CBV maps with flat detector CT. Clinical patient studies showed a high correlation of the C-arm CBV maps to CBV maps acquired with CTP (Struffert et al. 2010, Struffert et al. 2011, Struffert et al. 2012). However, CBV maps are limited to depict the infarct core but not the full extent of ischemic tissue. Therefore, the development of time-resolved perfusion flat detector imaging is desirable.

FD-CTP is challenging, since common C-arm systems are not able to rotate continuously by more than 360° and typically need $\sim 5\,\mathrm{s}$ to acquire one volume. This limits the temporal resolution of the acquired TCCs. Furthermore, perfusion imaging

is highly sensitive to noise, since the peaks of the TCCs inside the brain tissue typically lie in a range of 5–30 HU. Recently, novel techniques to overcome these challenges were proposed. Fieselmann et al. (Fieselmann et al. 2012) introduced a scanning protocol combining interleaved scanning and partial reconstruction interpolation for improved temporal sampling of TCCs. However, this approach requires multiple scanning sequences, which increases radiation and contrast agent dose to the patient and limits its clinical applicability. Wagner et al. (Wagner et al. 2013), Neukirchen et al. (Neukirchen et al. 2010) and Manhart et al. (Manhart, Kowarschik, Fieselmann, Deuerling-Zheng, Royalty, Maier & Hornegger 2013) presented dynamic algebraic reconstruction algorithms to reconstruct TCCs with increased temporal resolution from the acquired X-ray projection data by modelling the TCCs using gamma-variate functions (Wagner et al.) as well as Gaussian (Neukirchen et al.) and spline (Manhart et al.) basis functions. The algebraic approaches have a high computational effort and are sensitive to patient motion, because they rely on subtraction of mask projection data with static anatomical structures, e.g., skull and brain tissue, from the projection data with contrast agent enhancement. If the patient head moves during the projection data acquisition, the compensation of the 3D head movement on the 2D projection data is particularly difficult. These limitations may impede their application in clinical practice.

A novel possibility to acquire TCCs with improved temporal resolution are robotic C-arm systems (Artis zeego, Siemens AG, Germany). The Artis zeego system provides a high speed protocol (HSP) with increased C-arm rotation speed of up to 100°/s, thus allowing for the acquisition of projection data for one brain volume in less than 3 s. Royalty et al. (Royalty et al. 2013) evaluated the HSP in an experimental study measuring the brain perfusion of canines with induced focal ischemic regions. A strong correlation of FD-CTP maps to CTP maps as gold standard was reported. However, the results showed only a fair intra-observer performance in ischemic lesion mismatch detection and a consistent overestimation of CBF and CBV values in FD-CTP. Recently, Manhart et al. (Manhart, Fieselmann, Deuerling-Zheng & Kowarschik 2013) proposed the FDK-JBF reconstruction scheme based on Feldkamp (FDK) (Feldkamp et al. 1984) reconstruction followed by iterative denoising in volume space using joint bilateral filtering (JBF) (Petschnigg et al. 2004). The evaluation based on a digital brain phantom (Riordan et al. 2011) study showed the potential of the FDK-JBF approach to improve the noise reduction in brain tissue and to reduce the CBV and CBF overestimation. Furthermore, the FDK-JBF technique produced brain perfusion maps with a quality comparable to computationally more expensive algebraic reconstruction techniques, e.g., based on total variation (TV) minimization (Ritschl et al. 2011). However, motion of the patient's head was not considered in this study. It is likely that the patient moves during the acquisition procedure, especially because there is a pause of ~ 10 s between the acquisition of the mask projection images and the bolus projection images (with contrast agent enhancement). During the pause the contrast medium is injected intravenously and transported to the intracranial arteries. In a recent publication (Manhart, Aichert, Kowarschik, Deuerling-Zheng, Struffert, Doerfler, Maier & Hornegger 2013),

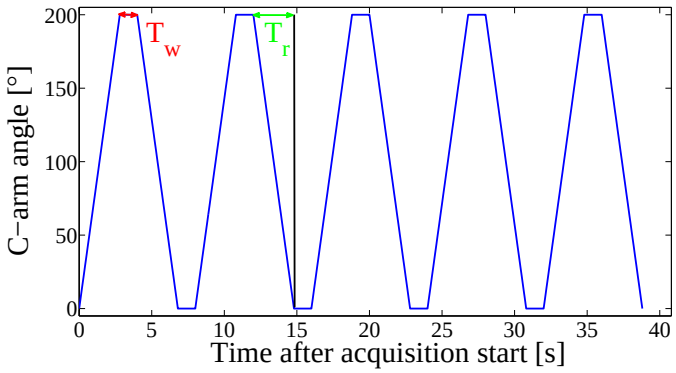

Figure 1: C-arm position during bolus volume acquisitions using the high speed FD-CTP protocol.

we discussed that this motion can cause severe artefacts in the perfusion maps. Due to limitations in the detector read-out rate, the angular sampling of the projection data in high speed scanning is coarse. This leads to streak artefacts in the reconstructed volumes. Mask volumes with static anatomical structures are subtracted from the volumes with contrast agent enhancement to compute volumes with pure contrast agent enhancement (bolus volumes). The streaks vanish in the bolus volumes since they are mainly caused by the patient's skull and are similar in the mask volumes and the volumes with contrast agent enhancement. If patient motion occurs between the C-arm rotations, it can be compensated by rigid registration. However, the streaks will not cancel out during subtraction in case of even slight errors in registration due to their high frequency structure. In (Manhart, Aichert, Kowarschik, Deuerling-Zheng, Struffert, Doerfler, Maier & Hornegger 2013), we described the FDK-SR-JBF technique, which extends the FDK-JBF approach by a streak removal (SR) for FD-CTP data. This work discusses our streak and noise reduction algorithm in more detail, includes alternative techniques in the evaluation (e.g., the TIPS filter (Mendrik et al. 2011)), and shows an additional patient study case with pre- and post-treatment acquisition.

This article is organized as follows. First, the acquisition process and protocols are detailed. Second, the novel reconstruction and filtering algorithm is described in detail and an overview of the alternative approaches used in the evaluation is provided. Finally, the FDK-SR-JBF approach is evaluated in comparison to the alternative methods with numerical brain phantom data and clinical patient data.

2. Methods

2.1. High Speed Acquisition Protocol

Unlike traditional CT gantries, current C-arm systems cannot rotate continuously around the patient multiple times. In order to perform time-resolved imaging, it is therefore necessary to rotate in a bi-directional manner, following a forward-backward

view-angle increment	1.5°
number of views per rotation	248
angular range per rotation	198°
time per rotation (T_r)	2.6/2.8 s
time between rotations (T_w)	1/1.2 s
number of rotations (N_rot)	7/10
source-to-detector distance	1200 mm
detector pixel size	0.616×0.616 mm^2
number of detector pixels	616×480
	after 4×4 re-binning
total detector size	$\approx 380 \times 296$ mm^2
tube peak voltage	82 kVp
system dose	1.2 μGy / projection

Table 1: Parameters of C-arm acquisition system.

pattern. The C-arm rotates multiple times in alternating directions and is forced to stop for a short period of time before it can turn around. Recent robotic C-arm systems are capable of performing a high speed protocol (HSP) (Artis zeego, Siemens AG, Germany). Each rotation of the HSP scan acquires 133 projections over a 198° angular range and requires $T_\mathrm{r} = 2.6 - 2.8\,\mathrm{s}$ for data acquisition with a pause of $T_\mathrm{w} = 1 - 1.2\,\mathrm{s}$ between any two successive rotations. Thus, TCCs can be acquired with a temporal sampling distance of $T_\mathrm{s} = T_\mathrm{r} + T_\mathrm{w} = 3.6 - 4\,\mathrm{s}$. First, mask projection images are acquired in a forward and a backward C-arm rotation before bolus injection. Mask projections in both directions are acquired because the positions of X-ray source and detector are not exactly the same for the forward and backward rotations. Subsequently, the contrast agent is injected intravenously. Finally, when the contrast bolus reaches the brain, the time series of bolus volumes is acquired in $N_\mathrm{rot} = 7$ or $N_\mathrm{rot} = 10$ consecutive rotations. Figure 1 shows a visualization of the HSP for the bolus volumes acquisition. Due to changes in the prototype C-arm control software between the studies, the protocol parameters differ slightly for the different experiments. Table 1 shows an overview of the acquisition parameters.

2.2. Algorithm Overview

To generate the perfusion information each rotation is reconstructed individually. Both FDK-JBF (Manhart, Fieselmann, Deuerling-Zheng & Kowarschik 2013) and FDK-SR-JBF (Manhart, Aichert, Kowarschik, Deuerling-Zheng, Struffert, Doerfler, Maier & Hornegger 2013) algorithms use standard FDK reconstruction complemented by volume-space post-processing. Figure 2 and Algorithm 1 show an overview of the algorithms constituting reconstruction with motion compensation and mask volume subtraction (Steps 1-3), JBF denoising (Steps 4-7 and 13-15), as well as streak artefact detection

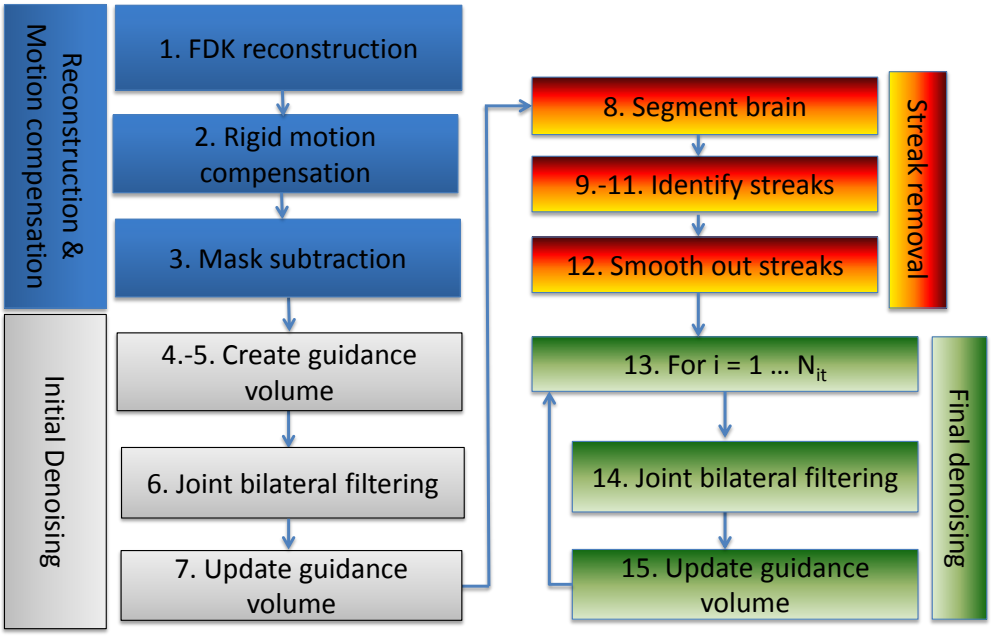

Figure 2: Flow chart of the FDK-SR-JBF algorithm.

and removal (Steps 8-12). Steps 6-12 are only applied by the FDK-SR-JBF algorithm.

We optimize the algorithm for several criteria. First, the tissue regions with the low-contrast perfusion information must be denoised. Second, blood vessels may not be blurred into the tissue, because this would lead to an over-estimation of contrast agent in the tissue and an under-estimation of contrast agent in the vessels. This in turn would cause an overall overestimation of blood flow and blood volume in the perfusion maps. Additionally, the algorithm needs to be resilient to artefacts, especially streaks. The single steps of the algorithm are discussed in detail below.

2.2.1. Reconstruction & Motion Compensation In Step 1 all mask and bolus acquisitions are reconstructed using a dedicated C-arm reconstruction algorithm (Wiesent et al. 2000), which is based on the cone-beam reconstruction algorithm by Feldkamp, Davis and Kress (FDK) (Feldkamp et al. 1984) in combination with Parker short scan weights (Parker 1982). This results in two mask volumes and 7 or 10 volumes with contrast agent enhancement. A non-smoothing Shepp-Logan filter kernel (Shepp & Logan 1974) is used to preserve the edges around the high contrast vessels.

All reconstructed volumes are registered to the forward mask volume in Step 2 using 3D-3D rigid registration (Viola & Wells III 1997) to compensate for possible patient head motion during the $\sim 50 - 60\,\mathrm{s}$ acquisition time.

In Step 3, the mask volumes are subtracted from the contrast agent enhanced volumes to obtain the bolus volumes. Any misalignment between mask and bolus volumes leads to incorrect attenuation values and dominates the slight contrast changes in tissue. In the ideal case, the subtraction removes the patient anatomy (i.e.,

Algorithm 1: FDK-SR-JBF Reconstruction Algorithm

Data: Pre-processed mask and bolus projection data
Result: Bolus volumes with reduced noise and streak artefacts

1 FDK reconstruction of mask and bolus acquisitions
2 Motion compensation by rigid 3D-3D registration
3 Compute bolus volumes by mask volume subtraction
4 Compute temporal maximum intensity projection M
5 Bilateral filtering of M with parameters σ_{S} and σ_{R0}
6 Initial joint bilateral filtering of bolus volumes with guidance image M and parameters σ_{S} and σ_{R} (Result only used for streak detection)
7 Re-compute M from filtered volumes
8 Segment brain tissue by thresholding mask volume (Thresholds: τ_{Air} and τ_{Bone})
9 Identify vessels and streaks by thresholding M (Thresholds: $\tau_{\mathrm{M\_min}}$ and $\tau_{\mathrm{M\_max}}$) and time curve analysis (Parameters: ν_{local} and ν_{global})
10 Identify additional streaks by thresholding $\mathrm{TV}(M)$ (Threshold: τ_{TV})
11 Combine streak and vessel masks
12 Remove streaks in M by smoothing
13 **for** $k = 1 \ldots N_{it}$ **do**
14 | Joint bilateral filtering of bolus volumes with guidance image M and parameters σ_{S} and σ_{R}
15 | Re-compute M from filtered volumes
16 **end**

bones, tissue) and reconstruction artefacts, leaving nothing but the contrasted agent enhancement and noise. Streak artefacts due to the low angular sampling in the mask and bolus volumes are identical, because they depend on the projection geometry and location of high contrast structures. However, if the patient moves and the registration step compensates for that motion, these artefacts will not cancel out.

2.2.2. Joint Bilateral Filtering The Shepp-Logan filter kernel from Step 1 yields sharp vessel edges, but a high noise level in the contrast agent enhancement of the tissue. To denoise the tissue regions a filtering scheme specific to the 3D+t perfusion data based on the joint bilateral filter (JBF) (Petschnigg et al. 2004) is used. The original bilateral filter (Aurich & Weule 1995, Tomasi & Manduchi 1998) is a popular non-linear edge-preserving noise reduction filter. The JBF is an extension of the bilateral filter, where the edge preservation is controlled by an additional guidance image. Each intensity of the filtered image $I'(\mathbf{p})$ at spatial location $\mathbf{p}$ is computed as a weighted average of the intensities of the original image $I(\mathbf{p})$ in a spatial neighbourhood $\mathcal{N}_{\mathbf{p}}$

$$I'(\mathbf{p}) = \frac{\sum\limits_{o \in \mathcal{N}_{\mathbf{p}}} I(\mathbf{p}+\mathbf{o}) \mathcal{W}_M(\mathbf{p}, \mathbf{o})}{\sum\limits_{o \in \mathcal{N}_{\mathbf{p}}} \mathcal{W}_M(\mathbf{p}, \mathbf{o})}, \tag{1}$$

$$\text{with } \mathcal{W}_M(\mathbf{p},\mathbf{o}) = \mathcal{G}_{\sigma_\mathrm{R}}\left(M(\mathbf{p}) - M(\mathbf{p}+\mathbf{o})\right) \cdot \mathcal{G}_{\sigma_\mathrm{D}}(\mathbf{p}-\mathbf{o}), \tag{2}$$

where $\mathcal{G}_\sigma(\mathbf{x}) = \exp\left(-0.5 \cdot \|\mathbf{x}\|_2^2/\sigma^2\right)$ denotes a Gaussian kernel. The weighting term $\mathcal{W}_M$ consists of the spatial closeness term $\mathcal{G}_{\sigma_\mathrm{D}}(\mathbf{p}-\mathbf{o})$ controlled by the domain parameter σ_D and the range similarity term $\mathcal{G}_{\sigma_\mathrm{R}}\left(M(\mathbf{p}) - M(\mathbf{p}+\mathbf{o})\right)$ controlled by the range parameter σ_R and by the guidance image M. The smoothing kernel locally adapts its shape while the image is being convolved. The range parameter controls how well edges of a specific contrast difference will be preserved. The joint bilateral filter corresponds to the bilateral filter, if the guidance image M is equal to the image I being filtered.

2.2.3. Joint Bilateral Filtering for Time-Concentration Curves The guidance volume M for JBF of the bolus volumes is defined by the temporal maximum intensity projection (MIP) of the bolus volumes. Therefore the maximum contrast agent attenuation in temporal direction is computed in Step 4 of Algorithm 1. The temporal MIP contains sharp edges for vessels, but is very noisy and streaky in the tissue regions (Figure 3a). Therefore, M is denoised by bilateral filtering with range variance $\sigma_{\mathrm{R}0}^2$ and domain variance σ_D^2 in Step 5. Figure 3b shows an example of M after bilateral filtering. In addition to the vessels, the guidance volume M can contain edges due to streak artefacts. These false edges need to be detected and removed, otherwise they will be translated to the filtered bolus volumes.

2.2.4. Streak Detection and Removal For streak detection, first a series of denoised bolus volumes is created by joint bilateral filtering of each bolus volume with range variance σ_R^2 and domain variance σ_D^2 in Step 6. Afterwards the guidance volume M is updated from the denoised series in Step 7. This series is only used for the streak detection described below, where denoised data is required for the TCC analysis.

Voxels in M that are affected by streaks are identified based on their contrast intensity and the shape of the TCC at the voxel position. Initially, we segment the forward mask volume into air, bone, and tissue by thresholding in Step 8. Voxels with a radiodensity below τ_Air are classified as air, voxels with a radiodensity above τ_Bone are classified as bone, and the remaining voxels are classified as brain tissue. To avoid misclassification by noise and artefacts, the mask volume is filtered by a 3D Gaussian kernel with domain variance σ_D^2 before thresholding. Subsequently, streaks and vessels are identified in Step 9 by thresholding M followed by TCC analysis.

Therefore a tissue voxel in M is classified as streak, if its intensity is below $\tau_{\mathrm{M\_min}} \leq 0$. No negative radiodensity values are expected, except slightly negative values due to noise, registration errors or artefacts. If a tissue voxel in M has a large intensity above a threshold $\tau_{\mathrm{M\_max}}$, it can belong to either a vessel or a streak. To differentiate between vessels and streaks, the TCCs are analysed. Vessels have typical TCCs with monotonic increase up to a clear contrast peak and possibly a second smaller peak due to second pass, while streaks produce irregular TCCs. Figure 4 shows a typical arterial TCC compared to a TCC observed at a streak. We denote the difference

between the peak value and the value from which the monotonic increase to the peak starts as uptake μ. Figure 4 shows the uptake of the dominant peak of an arterial TCC. To differentiate streaks and vessels, a voxel is heuristically identified as vessel if its corresponding TCC has:

1. a single global peak with an uptake μ_{global} of at least $\nu_{\text{global}} = 70\,\%$ of the peak value itself,
2. no further peak with an uptake μ_{local} of more than $\nu_{\text{local}} = 30\,\%$ of the global peak uptake μ_{global}.

Otherwise, this voxel is classified as streak.

Step 10 classifies tissue voxels of all other intensities as streaks if they have a total variation (TV) above τ_{TV}. The final brain segmentation is generated in Step 11 by combining the detected streaks and vessels. First a slice wise dilation operation on the segmented vessels using a 2D rectangular element of size 3×3 voxels is applied. The dilation of the vessels ensures that the vessel edges are preserved in the streak removal step. Then a slice wise erosion (1×2 element) followed by dilation (2×2 element) operation is applied to the streak mask to remove single outliers and close gaps in the detected streak areas. Finally, the brain segmentation is created by combining the vessel and streak masks with the initial brain tissue segmentation. If a voxel is identified as streak and vessel after dilation, it is classified as vessel. An example segmentation result is shown in Figure 3c. In Step 12, the identified streaks are removed by smoothing with a truncated 3D Gaussian kernel with domain variance σ_{D}^2 averaging over spatial close tissue voxels which are not classified as vessels.

Figure 3d shows M after the streak reduction was applied. The most pronounced streaks are removed, while the edges of all vessel structures except one smaller vessel are preserved. However, some less dominant streak structures are still preserved.

Finally, $N_{\text{JBF}} = 3$ JBF denoising iterations are applied on the original bolus data in Steps 13-15. The streak-reduced M is used as the initial guidance image. To handle the remaining artefacts, M updated in each iteration by recomputing the temporal MIP. Figure 3e shows the final MIP after the last JBF iteration with smooth tissue regions and sharp edges at the vessels.

2.3. Parameters of FDK-SR-JBF algorithm

Table 2 shows the parameters of the reconstruction algorithm used in the evaluation. The range variance of the JBF filter σ_{R}^2 was reduced to 10 HU in the simulation studies, since a range variance of 20 HU had already smoothed out many of the streaks in the simulation data.

2.4. Alternative Methods for Noise and Artefact Reduction

We compare our FDK-SR-JBF approach with the FDK-JBF approach (leaving out the streak removal steps) and other basic and state of the art approaches. The approaches are based on the algorithm shown in Figure 2 with the modifications described below.

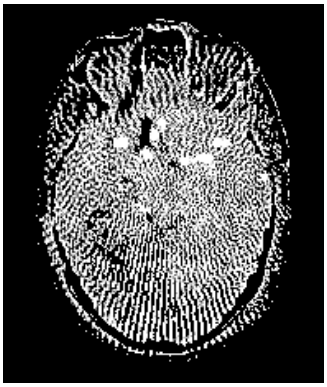

(a) Original temporal MIP.

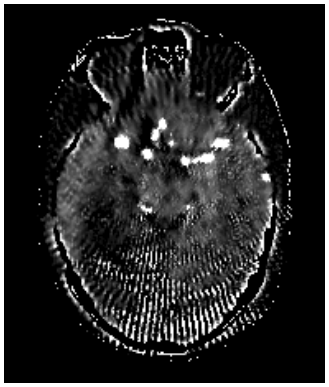

(b) Guidance volume M after bilateral filtering.

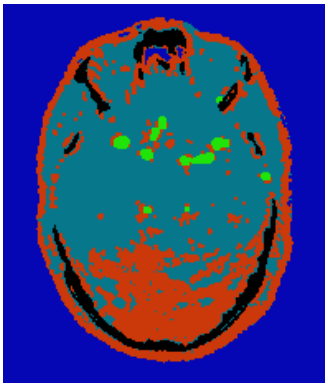

(c) Segmentation of M with streaks.

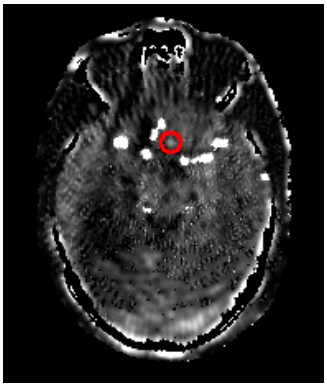

(d) Guidance volume M after streak removal. Red circle: blurred vessel.

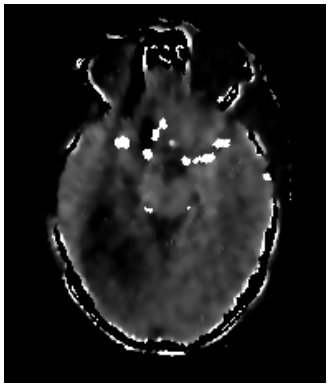

(e) Final guidance image M after JBF iterations.

Figure 3: Slice from temporal MIP (a) M before bilateral filtering, (b) after bilateral filtering, (c) segmentation of bilateral filtered M, (d) M after streak removal, and (e) M after all JBF iterations. Segmentation legend: orange: streaks, light green: vessels, dark green: tissue, black: bone, blue: air. Window: [0 50] HU.

Parameter	Value	Parameter	Value
JBF kernel size	$7 \times 7 \times 7$ voxels	$\tau_{\mathrm{M\_min}}$	-5 ΔHU
σ_{D}	1.5 mm	$\tau_{\mathrm{M\_max}}$	150 ΔHU
σ_{R}	20 HU (clinical data) 10 HU (simulation data)	τ_{TV}	20 ΔHU
σ_{R0}	120 HU	ν_{global}	70 %
τ_{Air}	- 800 HU	ν_{local}	30 %
τ_{Bone}	350	σ_{G}	2 mm
N_{it}	3		

Table 2: FDK-SR-JBF algorithm parameters.

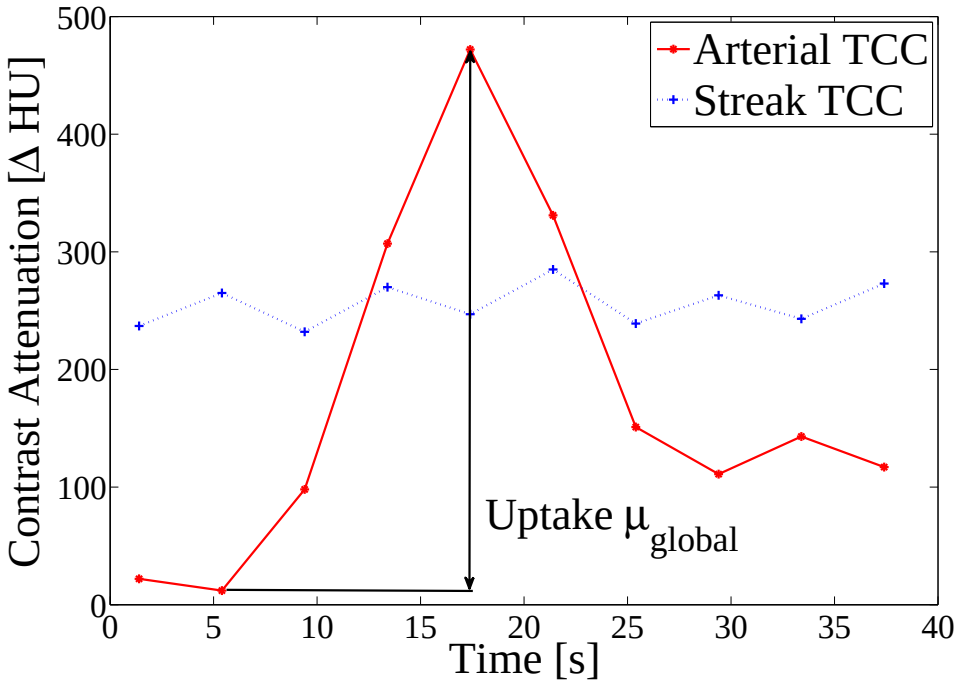

Figure 4: Time-concentration curves in an artery and in streak-affected brain tissue.

2.4.1. Smooth FDK Filter Kernel (FDK-SMOOTH) The denoising and streak removal parts are omitted. Noise is reduced by applying the FDK algorithm with a smooth filter kernel (Shepp-Logan kernel multiplied with a Gaussian kernel with $\sigma_{\mathrm{D}} = 1.25$ pixel).

2.4.2. 3D Gauss Filter (FDK-GAUSS) The streak removal parts are omitted and noise reduction is provided by a single iteration of 3D Gauss filtering ($\sigma_{\mathrm{D}} = 1.25\,\mathrm{mm}$) of all bolus volumes.

2.4.3. TIPS Filter (FDK-TIPS-1/FDK-TIPS-3) The streak removal parts are omitted. For noise reduction the time-intensity profile similarity (TIPS) filter (Mendrik et al. 2011) is applied, which was originally introduced for CTP data. The TIPS filter is also based on the bilateral filter defined in Equation 1. For the range closeness between neighbouring voxels, it uses the sum of squared differences (SSD) of the corresponding TCCs. Thus the range similarity term $\mathcal{G}_{\sigma_{\mathrm{R}}}$ in Equation 2 is replaced by the TIPS similarity term

$$\mathcal{G}_{\sigma_{\mathrm{TIPS}}}(\mathbf{p},\mathbf{o}) = \exp\left(-\frac{1}{2}\left(\frac{1}{N_{\mathrm{rot}}}\sum_{t=1}^{N_{\mathrm{rot}}}\left(I_t(\mathbf{p}) - I_t(\mathbf{p}+\mathbf{o})\right)^2/\sigma_{\mathrm{TIPS}}\right)^2\right), \quad (3)$$

where σ_{TIPS} denotes the TIPS parameter and I_t, $t = 1 \ldots N_{\mathrm{rot}}$ the t-th acquired bolus volume. One single application of the TIPS filter is denoted by FDK-TIPS-1. Similar as the JBF filter, we also iterated the TIPS filter $N_{\mathrm{TIPS}} = 3$ times due to the high noise and artefact level of the FD-CTP data. This approach is denoted as FDK-TIPS-3.

The selection of the TIPS parameter for the simulation study was done similarly to (Mendrik et al. 2011) by measuring the average SSD of the TCCs in the cerebral spinal fluid (CSF) located in the ventricles of the digital brain phantom. For the initial noise reduction, a TIPS parameter of $\sigma_{\mathrm{TIPS0}} = 3119\,\Delta\mathrm{HU}$ was determined. For the further iterations, a TIPS parameter of $\sigma_{\mathrm{TIPS}} = 615\,\Delta\mathrm{HU}$ was used, which was determined by the average SSD in the CSF after the initial TIPS denoising. Similarly to the JBF range parameter, we doubled the TIPS parameter for further iterations to $\sigma_{\mathrm{TIPS}} = 1230\,\Delta\mathrm{HU}$ for the clinical data.

2.4.4. Algebraic Reconstruction (OS-TV) The denoising and streak removal parts are omitted and the FDK reconstruction is replaced by a TV-based algebraic reconstruction approach with ordered subsets (OS). The OS-TV uses the algebraic reconstruction framework from (Manhart, Fieselmann, Deuerling-Zheng & Kowarschik 2013), performs 8 full iterations and applies TV regularization with automatic adaption of the TV gradient step size as proposed in the iTV algorithm (Ritschl et al. 2011). The automatic adaption assures improved data consistency after each iteration. The projections are partitioned into 10 disjoint subsets for the data consistency update to improve the convergence speed.

2.5. Perfusion Parameter Calculation

To compute the perfusion parameters, the reconstructed TCCs are sampled with a temporal resolution of 1 s by cubic spline interpolation using the denoised bolus volumes. Each bolus volume represents TCC samples at the mid time point of its acquisition. Our perfusion analysis software calculated the CBF, CBV, and MTT maps using the truncated SVD algorithm (Fieselmann et al. 2011) based on the indicator-dilution theory (Østergaard et al. 1996). The TTP maps were computed by determining the time from the beginning of the rise of the arterial input function to the peak of the TCC. For robust peak detection in noisy TCCs, a cubic Savitzky-Golay filter (Savitzky & Golay 1964) with a size of 25 temporal samples was applied prior to the peak search. No partial volume correction needs to be applied, because the spatial resolution of flat detector C-arm systems is almost isotropic and no axial blurring of arteries arises.

3. Evaluation

3.1. Digital Brain Perfusion Phantom Study

3.1.1. Phantom Description To evaluate the streak reduction technique in a simulation study we use the digital brain perfusion phantom from our previous work (Manhart, Kowarschik, Fieselmann, Deuerling-Zheng, Royalty, Maier & Hornegger 2013), which was originally proposed by Riordan et al. (Riordan et al. 2011). The phantom structure is based on the segmentation of MR data from a healthy human volunteer using the Freesurfer software (Dale et al. 1999). Thus it has a similar complexity as a clinical

	Healthy		Reduced CBF		Severely Reduced CBF/CBV	
	WM	GM	WM	GM	WM	GM
CBF [ml/100 g/min]	25 ± 14	53 ± 14	7.5 ± 4.25	16 ± 4.25	2.5 ± 1.4	5.3 ± 1.4
CBV [ml/100 g]	1.9 ± 0.9	3.3 ± 0.4	1.7 ± 0.9	3 ± 0.7	0.42 ± 0.2	0.71 ± 0.12
MTT [s]	4.6 ± 0.7	3.7 ± 0.7	14 ± 0.75	11 ± 0.75	10 ± 1	8 ± 1

Table 3: Perfusion parameters for digital brain phantom (WM = white matter, GM = grey matter).

brain perfusion scan and permits a realistic evaluation of algorithms applying non-linear filters. Inside the segmented brain, different tissue classes were annotated manually: healthy tissue, tissue with reduced CBF, and tissue with severely reduced CBF and CBV. The perfusion parameters were assigned to the annotated classes according to Table 3. The tissue TCCs were created from the assigned perfusion parameters by using a real measured arterial input function (AIF) from clinical CTP and the indicator-dilution theory. To reduce the homogeneity of the brain phantom, the MR data was used to vary the perfusion parameters. We incorporated the cortical bone structures of a human skull for a realistic simulation of streak artefacts. The skull was generated from a dedicated MR scan sequence of a human brain using the MR skull segmentation algorithm by Navalpakkam et al. (Navalpakkam et al. 2013). Patient motion was simulated by rotation of the bolus volumes by 2° relative to the mask volume around the z axis before generating the projection data. More details on the phantom design are described in (Aichert et al. 2013) and on the phantom web page ‡.

3.1.2. Experimental Setup We created dynamic C-arm projection data by forward projection of the 4D brain phantom according to the high speed protocol with $N_{\text{rot}} = 10$, 133 projections per rotation, rotation time $T_{\text{r}} = 2.8\,\text{s}$, and a pause time of $T_{\text{w}} = 1.2\,\text{s}$. Afterwards, Poisson-distributed noise was added to the projection data simulating an emitted X-ray density of $6 \cdot 10^5$ photons per mm^2 at the detector with a monochromatic photon energy of 60 keV.

For quantitative evaluation of the reconstructed perfusion maps, we calculated the Pearson correlation (PC) and the root mean square error (RMSE) between the reconstructed and the ground truth maps by applying an automated region of interest (ROI) analysis (Fieselmann et al. 2012). The slices of the perfusion maps with stroke annotation were partitioned into quadratic areas of 4×4 pixels. The average perfusion values of the ROIs were calculated and used for the PC and RMSE computation. ROIs containing vascular structures, bone, or air were ignored. All slices with stroke

‡ www5.cs.fau.de/data

annotation were used for the PC and RMSE calculation (altogether 50 slices and 28225 samples).

We measured the computation time for reconstruction and denoising of the simulation data on a workstation with 8 Intel(R) Xeon(R) W3565 CPUs with 3.20 GHz, 12 GB RAM, and an NVIDIA Quadro FX 5800 display adapter. The algorithms were implemented in the C++ programming language, with the most computationally expensive steps (forward projection, backward projection, and JBF) being computed on the graphics processing unit (GPU) and implemented using the NVIDIA CUDA programming language.

3.2. Human Clinical Datasets

The clinical datasets include three different FD-CTP acquisitions from two patients. The patients were both suffering from AIS and were treated by interventional intra-arterial recanalization with self-expanding stents. The first patient (69 year old male) was admitted due to an acute occlusion of the middle cerebral artery on the left. Corresponding to the side of occlusion the patient was suffering from hemiplegia of the right side of the body. A HSP FD-CTP acquisition was performed after successful recanalization with 7 rotations after contrast injection, 133 projections per rotation, rotation time $T_\mathrm{r} = 2.8\,\mathrm{s}$, and a pause of $T_\mathrm{w} = 1\,\mathrm{s}$.

The second patient (72 year old female) was admitted due to an occlusion of the vertebral artery on the left, including the posterior inferior cerebellar artery. Correspondingly, this patient presented clinical dizziness. Two HSP FD-CTP acquisitions were performed before and after successful recanalization with 10 rotations after contrast injection, 133 projections per rotation, rotation time $T_\mathrm{r} = 2.6\,\mathrm{s}$, and a pause of $T_\mathrm{w} = 1\,\mathrm{s}$.

3.3. Results

3.3.1. Digital Brain Phantom Dataset Figure 5 shows axial slices of reconstructed CBF maps compared to the ground truth map. The maps were reconstructed with the FDK-SMOOTH, FDK-GAUSS, FDK-JBF, FDK-TIPS-1 and FDK-TIPS-3 methods, respectively. Figure 6 shows axial slices from CBF, CBV, MTT, and TTP maps reconstructed with the FDK-SR-JBF and OS-TV algorithms and compared to the ground truth maps. The quantitative results are shown in Table 4. They compare the PC and RMSE of the reconstructed maps to the reference maps and the computation time for reconstruction and denoising on the workstation for the FDK-SR-JBF and OS-TV algorithms.

3.3.2. Clinical Stroke Case with Patient Motion Figure 7 shows axial slices of CBF maps reconstructed from HSP FD-CTP data of the first patient using the FDK-GAUSS, FDK-JBF, and FDK-TIPS-3 algorithms. Figure 8 shows slices of the CBF, CBV, MTT,

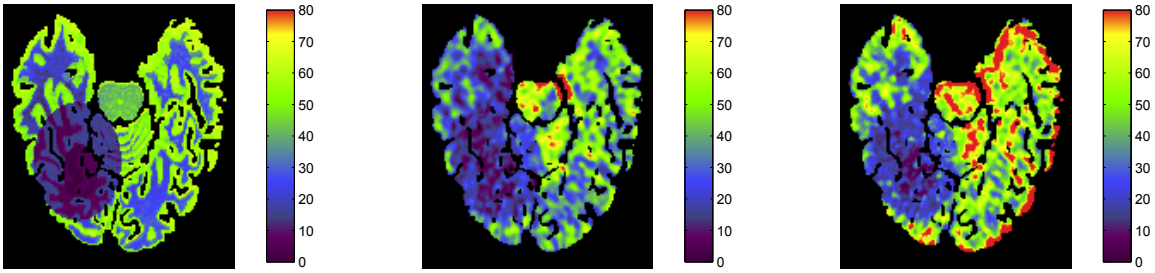

(a) Reference map (b) FDK-SMOOTH (c) FDK-GAUSS

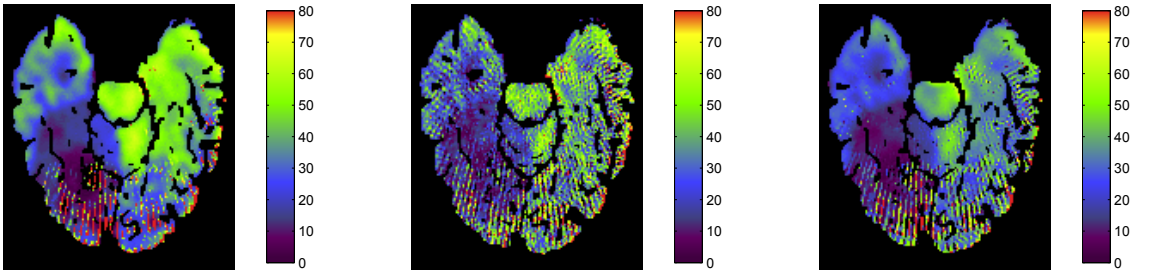

(d) FDK-JBF (e) FDK-TIPS-1 (f) FDK-TIPS-3

Figure 5: Axial slices of CBF maps created from numerical brain perfusion phantom FD-CTP data compared to the ground truth map (a) (units ml/100 g/min). Maps created from reconstructions with (b) FDK-SMOOTH, (c) FDK-GAUSS, (d) FDK-JBF, (e) FDK-TIPS-1, (f) FDK-TIPS-3. Axial position of slices relative to central slice is -26 mm.

	Pearson Correlation		RMSE	
	FDK-SR-JBF	OS-TV	FDK-SR-JBF	OS-TV
CBF	0.83	0.84	7.17 ml/100 g/min	5.94 ml/100 g/min
CBV	0.74	0.75	0.56 ml/100 g	0.85 ml/100 g
MTT	0.85	0.89	2.23 s	2.34 s
TTP	0.87	0.86	1.32 s	1.32 s
Computation Time	69 s	1610 s		

Table 4: Quantitative results of brain phantom study. Pearson correlation (PC) and root mean square error (RMSE) of CBF, CBV, MTT and TTP perfusion maps reconstructed with FDK-SR-JBF and OS-TV approaches to reference volumes.

and TTP perfusion maps in axial and coronal viewing directions. These maps were reconstructed with the FDK-SR-JBF and the OS-TV algorithms.

3.3.3. Clinical Stroke Case with Pre- and Post-Treatment Acquisition Figure 9 shows slices of CBF and CBV maps from HSP FD-CTP data acquired from the second patient. All maps were reconstructed with the FDK-SR-JBF approach. Maps displaying the

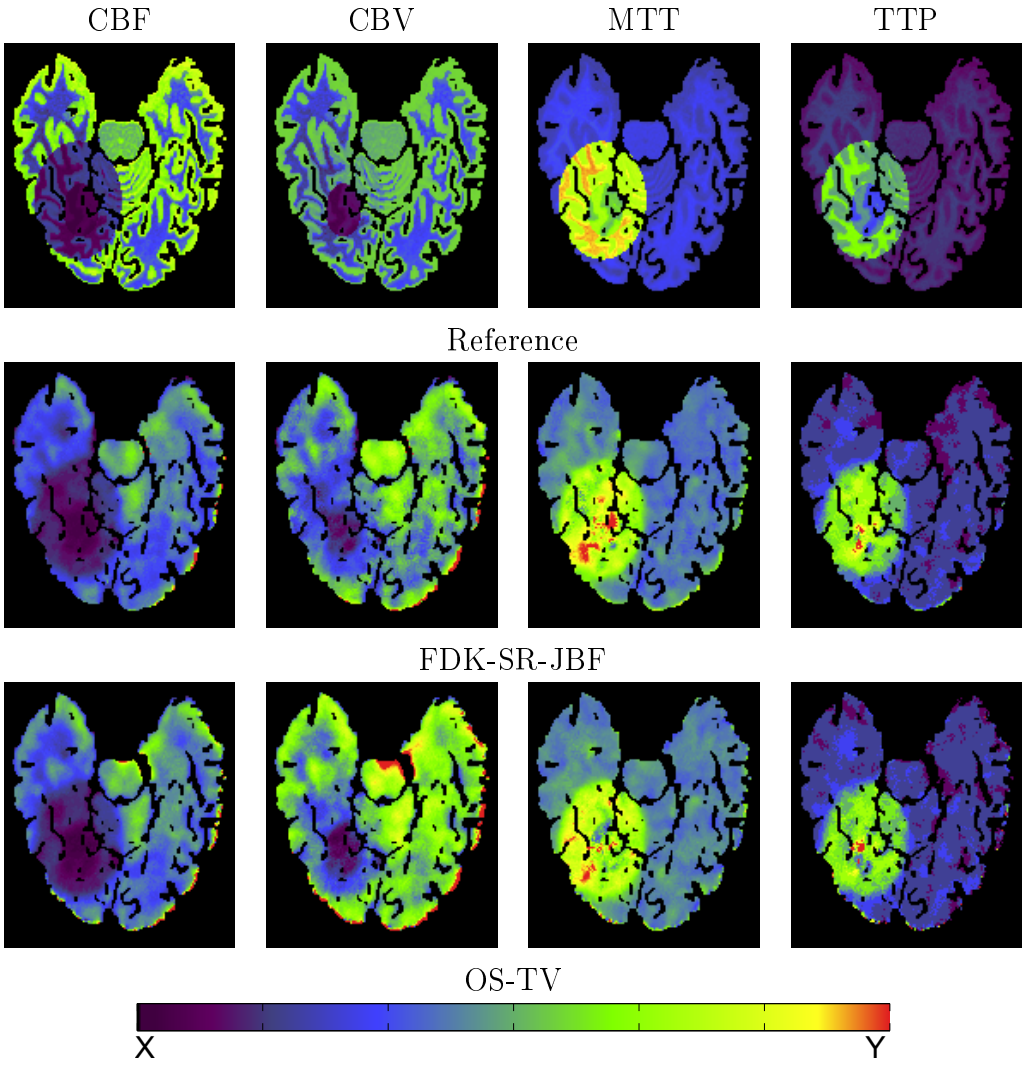

Figure 6: Axial slices of CBF, CBV, MTT and TTP maps reconstructed from brain perfusion phantom data with FDK-SR-JBF and OS-TV approaches compared to the ground truth. Map windows: CBF [X = 0, Y = 80] ml/100 g/min; CBV [0, 6] ml/100 g; MTT [0, 15] s, and TTP [13, 23] s. Axial position of the slices relative to central slice is -26 mm.

brain perfusion before (pre) and and after (post) successful recanalization are shown in axial and sagittal directions. The pre- and post-treatment perfusion maps where registered to each other using rigid registration. Axial slices from the cerebellum and the occipital lobes are shown. The cerebellum slices show stroke-affected tissue before and after successful treatment and the occipital lobe slices show healthy tissue and visualize the reproducibility of the HSP FD-CTP acquisition and reconstruction. Figure 10 shows the corresponding MTT and TTP maps.

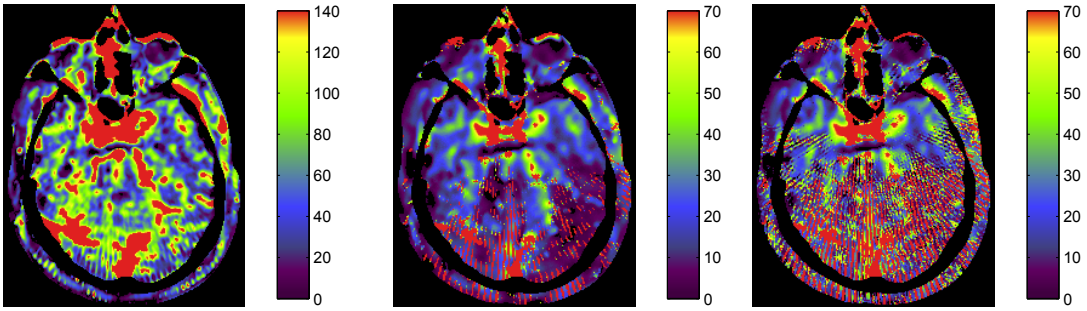

(a) FDK-GAUSS (b) FDK-JBF (c) FDK-TIPS-3

Figure 7: CBF maps created from clinical patient data with head motion using the FDK-GAUSS, FDK-JBF, and FDK-TIPS-3 approaches (units ml/100 g/min).

4. Discussion

The evaluated FDK-SR-JBF algorithm applies FDK reconstruction followed by guided noise reduction with JBF. The JBF guidance volume is computed from the temporal maximum intensity projection of the bolus volumes time series. To handle streak artefacts in the JBF guidance volume, a streak removal method is applied. Therefore, the brain is segmented into tissue, vessels, and streaks using information from the TCCs and total variation. Subsequently, the streaks are removed by smoothing the identified areas in the JBF guidance image. Finally, noise and artefacts are reduced in the bolus volumes by iteratively applying JBF using the streak-reduced guidance volume.

The evaluation is carried out with simulation data employing a digital brain perfusion phantom. Furthermore, we show perfusion maps reconstructed from three real clinical datasets from two different AIS patients. The FDK-SR-JBF technique is compared to alternative post-processing methods after FDK reconstruction and algebraic reconstruction with TV regularization.

The axial CBF slices reconstructed from the numerical phantom data shown in Figure 5 demonstrate that the alternative post-processing methods do not provide sufficient image quality. The perfusion maps created by FDK-SMOOTH and FDK-GAUSS are noisy and the edges at the high contrast vessels are blurred into the tissue. Furthermore, especially the 3D Gauss filtering causes a partial volume effect (i.e., an underestimation of the contrast agent enhancement in the vessels), which leads to an overestimation of the CBF values. The JBF and TIPS methods avoid the blurring of the vessels, but also preserve the edges caused by streak artefacts. The streaks are visible in the CBF maps and impede the visibility of the stroke affected area. These results are confirmed by the CBF maps created from the FD-CTP data of the first patient shown in Figure 7.

Sufficient noise and artefact reduction in combination with preserved edges at vessels is achieved by the FDK-SR-JBF and OS-TV approaches in the numerical perfusion maps shown in Figure 6 and the clinical perfusion maps shown in Figure

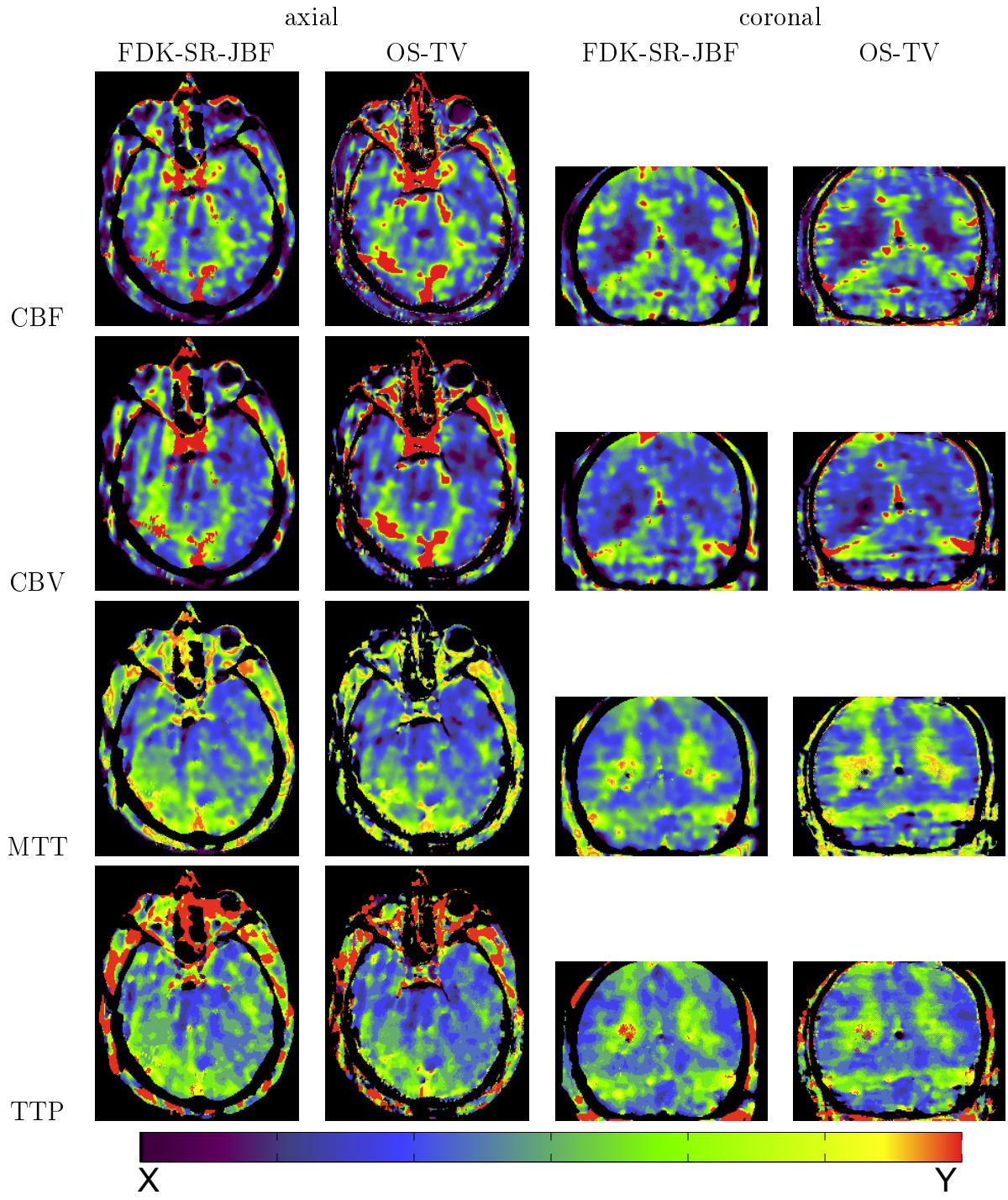

Figure 8: Axial and coronal slices of perfusion maps created from clinical patient data with head motion reconstructed with FDK-SR-JBF and OS-TV approaches. Windows: CBF [X = 0, Y = 80] ml/100 g/min; CBV [0, 8] ml/100 g; MTT [0, 12] s; TTP [12, 22] s. Axial position of slices relative to central slice: (axial) -56 mm; (coronal) -60 to +60 mm.

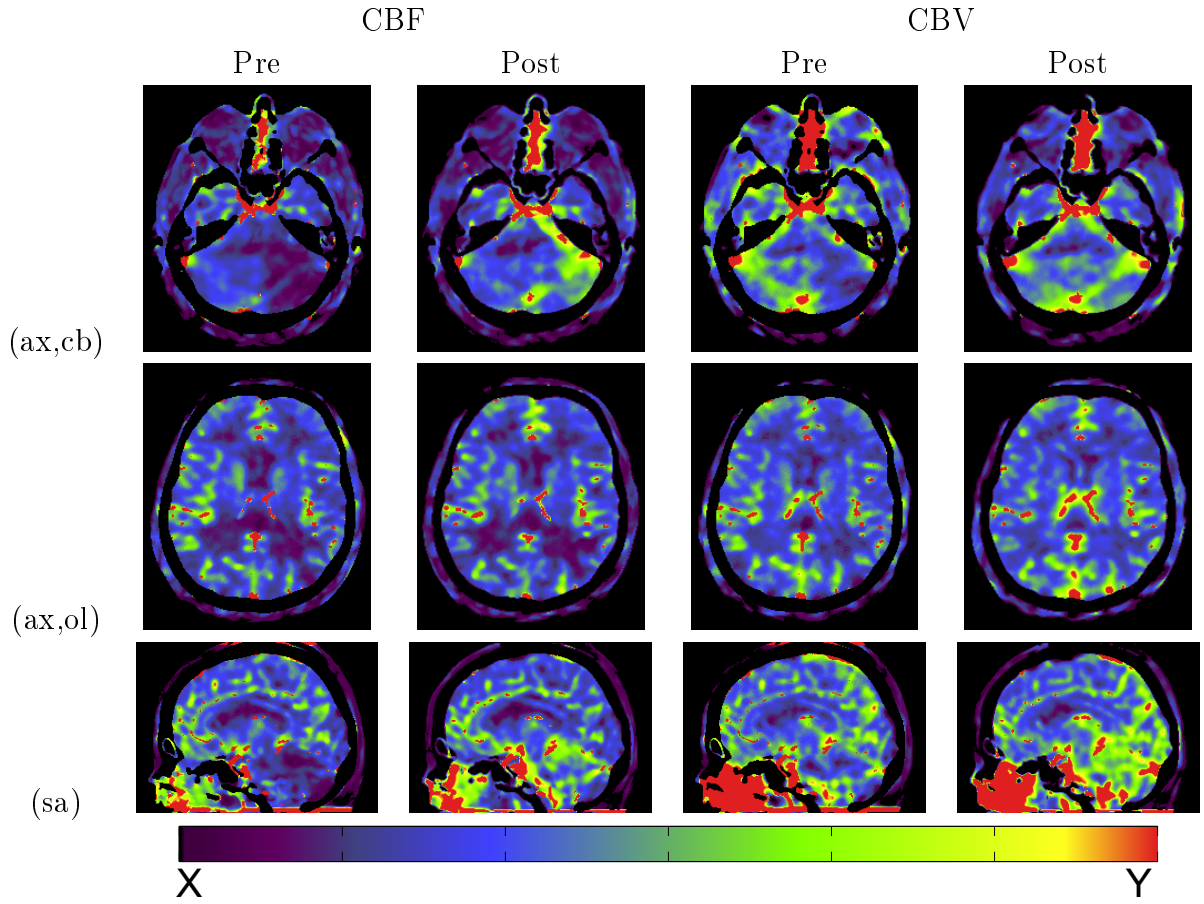

Figure 9: Axial (ax) and sagittal (sa) slices of CBF and CBV maps from a patient study with pre- and post-treatment acquisitions. Axial slices from cerebellum (cb) and occipital lobes (ol). Map windows pre-treatment acquisition: CBF [X = 0, Y = 80] ml/100 g/min; CBV [0, 8] ml/100 g. Map windows post-treatment acquisition: CBF [0, 60] ml/100 g/min; CBV [0, 6] ml/100 g. Axial position of the slices relative to central slice: (ax,cb) -70 mm; (ax,ol) -22 mm; (sa) -72 to +72 mm.

8. Both approaches provide similar visual quality. Also the quantitative results in Table 4 show similar PC and RMSE distance to the ground truth. However, the computation time of OS-TV is with 26 min 50 s by a factor of more than 23 higher than the computation time of FDK-SR-JBF with 1 min 9 s.

In the TTP and MTT brain phantom maps (Figure 6) the differentiation of the infarct core to the penumbra is lost. The contrast agent enhancement in the infarct core is very low (peak $\sim$ 5 HU) and therefore the contrast-to-noise (CNR) ratio is accordingly small. This affects the MTT and TTP parameters. As MTT = CBV/CBF, MTT gets numerically unstable if CBF very small (as in the infarct core). TTP relies on the detection of the TCC peak, which is difficult in case of very low CNR. However, the infarct core can still be depicted from the penumbra by the physician by comparing the CBV map showing the infarct core to the CBF, MTT, and TTP maps showing the full

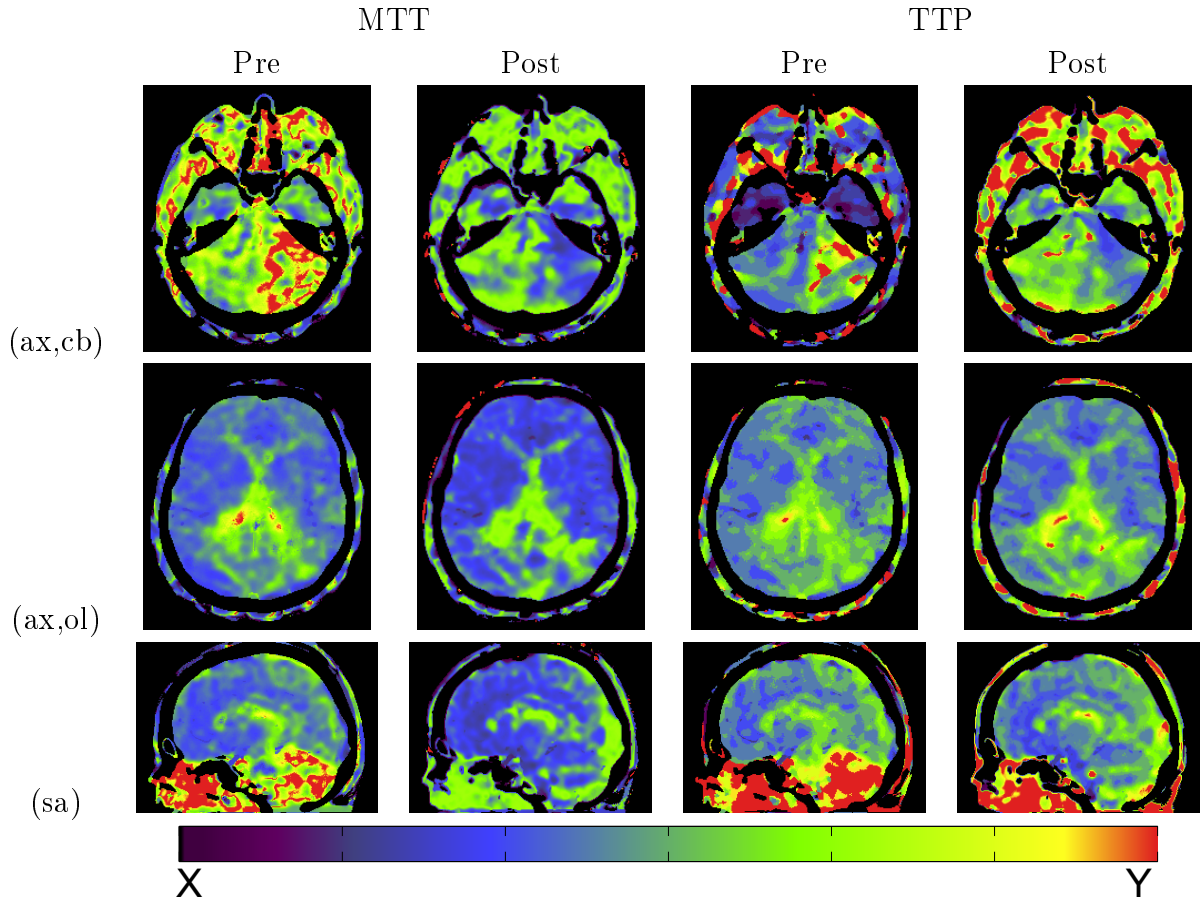

Figure 10: Axial (ax) and sagittal (sa) slices of MTT and TTP maps from a patient study with pre- and post-treatment acquisitions. Axial slices from cerebellum (cb) and occipital lobes (ol). Map windows pre-treatment acquisition: MTT [X = 0, Y = 16] s; TTP [10, 22] s (ol slice) and [14, 28] s (cb slice). Map windows post-treatment acquisition: MTT [0, 20] s; TTP [11, 25] s. Axial position of the slices relative to central slice: (ax,cb) -70 mm; (ax,ol) -22 mm; (sa) -72 to +72 mm.

infarct area.

The pre- and post-treatment perfusion maps of the second patient in Figures 9 and 10 provide physiological meaningful results. The pre-treatment maps clearly show a reduction of CBF and CBV and an increase of MTT and TTP in the left hemisphere of the cerebellum, which corresponds to the stroke-affected area. After successful recanalization of the cerebellum, the post-treatment maps show increased CBF and CBV and decreased MTT and TTP in the stroke-affected area. This corresponds to hyperperfusion, which is a common finding after recanalization in stroke. Furthermore, the perfusion maps of the occipital lobes of the brain, which were not affected by stroke and not subject to treatment, look very similar in the pre- and post-treatment maps. This supports the reproducibility of the proposed acquisition and reconstruction technique.

The FDK-SR-JBF approach produced suitable results in first simulation and real

data studies. The perfusion maps allow the physician to determine the infarct area with the infarct core and the penumbra. Furthermore, the computation speed of FDK-SR-JBF is sufficiently fast for interventional use on clinical workstations. Therefore it could be a suitable approach for interventional FD-CTP. However, our heuristic approach can likely fail to discern streaks and vessels at some voxels and some streak artefacts could be preserved or small vessels blurred (e.g., see Figure 3d). As long as the artefacts are limited to few voxels, the image quality of the perfusion maps is impaired, but the clinical value of the perfusion maps is not strongly affected.

One limitation of the evaluated noise and artefact reduction techniques for FD-CTP is that they can only handle the head motion which occurs between the acquisitions. Motion during one rotation of the C-arm will cause additional artefacts and might make the acquired volume unusable for the perfusion computation. Thus including online motion correction techniques (Debbeler et al. 2013, Wicklein et al. 2012) represents an important direction for future research. Furthermore, the usage of exact analytical reconstruction algorithms (Katsevich 2003, Defrise & Clack 1994) could help to improve the image quality in higher cone beam angles as they avoid the inexact handling of the cone beam projection data by the Feldkamp short scan algorithm.

5. Conclusions

The simulation and patient studies show the potential of the FDK-SR-JBF approach for providing viable FD-CTP maps. The FDK-SR-JBF approach produced perfusion maps with a quality comparable to an algebraic reconstruction technique based on total variation minimization, but the computation time is reduced by factor of more than 23 on a clinical workstation. The evaluation using the pre- and post-treatment acquisitions shows that interventional FD-CTP acquisition is feasible with FDK-SR-JBF reconstruction. However, further validation of the clinical applicability and robustness is required by a thorough quantitative comparison of C-arm perfusion maps to CT perfusion and MR perfusion and will be carried out in the future.

Acknowledgments

The authors gratefully acknowledge funding of the Medical Valley national leading edge cluster, Erlangen, Germany, diagnostic imaging network, sub-project BD 16, research grant nr. 13EX1212G. M. Manhart gratefully acknowledges funding from Siemens AG, Angiography & Interventional X-Ray Systems, Germany. Y. Deuerling-Zheng and M. Kowarschik are employed by Siemens AG, Healthcare Sector, Germany.

Disclaimer: The concepts and information presented in this paper are based on research and are not commercially available. The patient study has been approved by the ethics commission of the Medical Faculty at Friedrich-Alexander-Universität Erlangen-Nürnberg, Germany, Ethik-No. 4535 on Dec 14th 2011.

References

Ahmed A S, Zellerhoff M, Strother C, Pulfer K, Deuerling-Zheng Y, Redel T, Royalty K, Consigny D & Niemann D 2009 C-arm CT measurement of cerebral blood volume: An experimental study in canines *AJNR* **30**(5), 917–22.

Aichert A, Manhart M T, Navalpakkam B K, Grimm R, Hutter J, Maier A, Hornegger J & Doerfler A 2013 A realistic digital phantom for perfusion C-arm CT based on MRI data *in* 'Proc. IEEE NSS MIC 2013'. (accepted for presentation).

Aurich V & Weule J 1995 *in* G Sagerer, S Posch & F Kummert, eds, 'Mustererkennung 1995' Informatik aktuell Springer Berlin Heidelberg pp. 538–545.
`http://dx.doi.org/10.1007/978-3-642-79980-8_63`

Dale A M, Fischl B & Sereno M I 1999 Cortical surface-based analysis: I. Segmentation and surface reconstruction *NeuroImage* **9**(2), 179–194.

Debbeler C, Maass N, Elter M, Dennerlein F & Buzug T M 2013 A new CT rawdata redundancy measure applied to automated misalignment correction *in* 'Proc. 12th International Meeting on Fully Three-Dimensional Image Reconstruction in Radiology and Nuclear Medicine' Tahoe City, CA, USA pp. 264–267.

Defrise M & Clack R 1994 A cone-beam reconstruction algorithm using shift-variant filtering and cone-beam backprojection *Medical Imaging, IEEE Transactions on* **13**(1), 186–195.

Feldkamp L, Davis L & Kress J 1984 Practical cone-beam algorithm *Journal of the Optical Society of America A* **1**(6), 612–619.

Fieselmann A, Ganguly A, Deuerling-Zheng Y, Zellerhoff M, Rohkohl C, Boese J, Hornegger J & Fahrig R 2012 Interventional 4-D C-arm CT perfusion imaging using interleaved scanning and partial reconstruction interpolation *Medical Imaging, IEEE Transactions on* **31**(4), 892 – 906.

Fieselmann A, Kowarschik M, Ganguly A, Hornegger J & Fahrig R 2011 'Deconvolution-based CT and MR brain perfusion measurement: Theoretical model revisited and practical implementation details' International Journal of Biomedical Imaging. Article ID 467563.

Furlan A, Higashida R, Wechsler L, Gent M, Rowley H, Kase C, Pessin M, Ahuja A, Callahan F, Clark W M et al. 1999 Intra-arterial prourokinase for acute ischemic stroke *JAMA* **282**(21), 2003–2011.

Hacke W, Kaste M, Bluhmki E, Brozman M, Dávalos A, Guidetti D, Larrue V, Lees K R, Medeghri Z, Machnig T et al. 2008 Thrombolysis with alteplase 3 to 4.5 hours after acute ischemic stroke *New England Journal of Medicine* **359**(13), 1317–1329.

Katsevich A 2003 A general scheme for constructing inversion algorithms for cone beam ct *International Journal of Mathematics and Mathematical Sciences* **2003**(21), 1305–1321.

Manhart M T, Aichert A, Kowarschik M, Deuerling-Zheng Y, Struffert T, Doerfler A, Maier A K & Hornegger J 2013 Guided noise reduction with streak removal for high speed perfusion C-arm CT *in* 'Proc. IEEE NSS MIC 2013'. (accepted for presentation).

Manhart M T, Fieselmann A, Deuerling-Zheng Y & Kowarschik M 2013 Iterative denoising algorithms for perfusion C-arm CT with a rapid scanning protocol *in* 'Proc. IEEE ISBI 2013' San Francisco, CA, USA pp. 1223–1227.

Manhart M T, Kowarschik M, Fieselmann A, Deuerling-Zheng Y, Royalty K, Maier A K & Hornegger J 2013 Dynamic iterative reconstruction for interventional 4-D C-arm CT perfusion imaging *Medical Imaging, IEEE Transactions on* **32**(7), 1336–1348.

Mendrik A M, Vonken E, van Ginneken B, de Jong H W, Riordan A, van Seeters T, Smit E J, Viergever M A & Prokop M 2011 TIPS bilateral noise reduction in 4D CT perfusion scans produces high-quality cerebral blood flow maps *Physics in Medicine and Biology* **56**(13), 3857–3872.

Miles K A & Griffiths M R 2003 Perfusion CT: a worthwhile enhancement? *British Journal of Radiology* **76**(904), 220–231.

Navalpakkam B K, Braun H, Kuwert T & Quick H H 2013 Magnetic Resonance-Based Attenuation Correction for PET/MR Hybrid Imaging Using Continuous Valued Attenuation Maps *Invest Radiol* **48**(5), 323–332.

Neukirchen C, Giordano M & Wiesner S 2010 An iterative method for tomographic X-ray perfusion estimation in a decomposition model-based approach *Medical Physics* **37**(12), 6125–6141.

Parker D L 1982 Optimal short scan convolution reconstruction for fan beam CT *Medical Physics* **9**(2), 254–257.

Petschnigg G, Szeliski R, Agrawala M, Cohen M, Hoppe H & Toyama K 2004 Digital photography with flash and no-flash image pairs *ACM Transactions on Graphics (TOG)* **23**(3), 664–672.

Rha J H & Saver J L 2007 The impact of recanalization on ischemic stroke outcome a meta-analysis *Stroke* **38**(3), 967–973.

Riordan A J, Prokop M, Viergever M A, Dankbaar J W, Smit E J & de Jong H W A M 2011 Validation of CT brain perfusion methods using a realistic dynamic head phantom *Medical Physics* **38**(6), 3212–3221.

Ritschl L, Bergner F, Fleischmann C & Kachelrieß M 2011 Improved total variation-based CT image reconstruction applied to clinical data *Physics in Medicine and Biology* **56**(6), 1545–1561.

Royalty K, Manhart M, Pulfer K, Deuerling-Zheng Y, Strother C, Fieselmann A & Consigny D 2013 C-arm CT measurement of cerebral blood volume and cerebral blood flow using a novel high-speed acquisition and a single intravenous contrast injection *AJNR* -, –. (in press).

Savitzky A & Golay M J E 1964 Smoothing and differentiation of data by simplified least squares procedures *Analytical Chemistry* **36**(8), 1627–1639.

Shepp L A & Logan B F 1974 The Fourier reconstruction of a head section *Nuclear Science, IEEE Transactions on* **21**(3), 21–43.

Østergaard L, Weisskoff R M, Chesler, David A. Gyldensted C & Rosen B R 1996 High resolution measurement of cerebral blood flow using intravascular tracer bolus passages. Part I: Mathematical approach and statistical analysis *Magnetic Resonance in Medicine* **36**(5), 715–725.

Struffert T, Deuerling-Zheng Y, Engelhorn T, Kloska S, Gölitz P, Köhrmann M, Schwab S, Strother C & Doerfler A 2012 Feasibility of cerebral blood volume mapping by flat panel detector CT in the angiography suite: first experience in patients with acute middle cerebral artery occlusions *American Journal of Neuroradiology* **33**(4), 618–625.

Struffert T, Deuerling-Zheng Y, Kloska S, Engelhorn T, Boese J, Zellerhoff M, Schwab S & Doerfler A 2011 Cerebral blood volume imaging by flat detector computed tomography in comparison to conventional multislice perfusion CT *European Radiology* **21**(4), 882–889.

Struffert T, Deuerling-Zheng Y, Kloska S, Engelhorn T, Strother C, Kalender W, Köhrmann M, Schwab S & Doerfler A 2010 Flat detector CT in the evaluation of brain parenchyma, intracranial vasculature, and cerebral blood volume: a pilot study in patients with acute symptoms of cerebral ischemia *American Journal of Neuroradiology* **31**(8), 1462–1469.

Struffert T, Richter G, Engelhorn T, Doelken M, Goelitz P, Kalender W A, Ganslandt O & Doerfler A 2009 Visualisation of intracerebral haemorrhage with flat-detector CT compared to multislice CT: results in 44 cases *European radiology* **19**(3), 619–625.

Tomasi C & Manduchi R 1998 Bilateral filtering for gray and color images *in* 'Computer Vision, Sixth International Conference on' IEEE Washington, DC, USA pp. 839–846.

Viola P & Wells III W M 1997 Alignment by maximization of mutual information *International Journal of Computer Vision* **24**(2), 137–154.

Wagner M, Deuerling-Zheng Y, Möhlenbruch M, Bendszus M, Boese J & Heiland S 2013 A model based algorithm for perfusion estimation in interventional C-arm CT systems *Medical Physics* **40**(3), 0319161–03191611.

Wicklein J, Kunze H, Kalender W A & Kyriakou Y 2012 Image features for misalignment correction in medical flat-detector CT *Medical Physics* **39**, 4918.

Wiesent K, Barth K, Navab N, Durlak P, Brunner T, Schuetz O & Seissler W 2000 Enhanced 3-d-reconstruction algorithm for c-arm systems suitable for interventional procedures *Medical Imaging, IEEE Transactions on* **19**(5), 391–403.

Zaidat O O, Wolfe T, Hussain S I, Lynch J R, Gupta R, Delap J, Torbey M T & Fitzsimmons B F

2008 Interventional acute ischemic stroke therapy with intracranial self-expanding stent *Stroke* **39**(8), 2392–2395.